GNSS Array-Based Ionospheric Spatial Gradient Monitoring: Precision and Integrity Analysis

S. Zaminpardaz[1], P.J.G. Teunissen[1,2], N. Nadarajah[1] and A. Khodabandeh[1]
[1]*GNSS Research Centre, Curtin University of Technology, Perth, Australia*
[2]*Geoscience and Remote Sensing, Delft University of Technology, The Netherlands*

Biography

Safoora Zaminpardaz is a PhD student at Curtin's GNSS Research Centre. Her research interests comprise array-based multi-GNSS, ionosphere sensing and precise point positioning. Peter J.G. Teunissen is Professor of Geodesy and Navigation, and Head of Curtin's GNSS Research Centre. Nandakumaran Nadarajah and Amir Khodabandeh are, respectively, a postdoc research fellow and a PhD student at the GNSS Research Centre of Curtin University. Their research focus is on modeling next-generation GNSSs for precise positioning, navigation and attitude determination.

Abstract

Integrity monitoring and reliable detection of the ionospheric spatial gradient is of importance for various fields including total electron content modeling, radio communication and radar, and differential GNSS applications such as landing, departure and surface operations at an airport. In this contribution, we investigate the precision and the integrity of the ionospheric spatial gradient estimation upon the double-differenced (DD) array-based GNSS model of observations. Closed-form expressions for the variance matrix of the ionospheric spatial gradient and the corresponding uniformly most powerful invariant (UMPI) minimal detectable biases (MDBs) are provided for different scenarios, through which we assess the importance of several contributing factors. The closed-form expressions will show that the precision of the ionospheric spatial gradient estimator and its detectability are independent of our choice for the reference receiver and the reference satellite when forming the DD equations.

In this contribution it will be shown how the precision of the estimated ionospheric spatial gradient and its MDB depend on and benefit from the number of receivers, number of satellites, number of frequencies, and the size and geometry of the array.

1 Introduction

Acting as a dispersive environment, the ionosphere affects the GNSS measurements through introducing a delay in the code signals and an advance in the carrier-phase signals, see e.g. [1, 2]. Since the ionosphere varies in both space and time, the affected GNSS signals would therefore also experience spatial and temporal variations. Large values for the ionospheric spatial gradient are expected when an ionospheric front occurs. The possible undesirable impact of the ionospheric spatial gradients needs therefore to be properly taken into account. Indeed, integrity monitoring and reliable detection of the ionospheric spatial gradient have recently been given growing attention in various disciplines such as estimating and modeling total electron content [3–5], radio communication and radar [6], and differential GNSS applications such as landing, departure and surface operations at an airport [7–10]. In case of the aviation applications for instance, a single Ground Facility (GF), comprising multiple spatially-separated GNSS receivers, is meant to ensure safe flight operations through monitoring signal-in-space failures, e.g. ionospheric spatial gradient that are potentially hazardous for the user (aircraft) positioning.

In this contribution, we study the precision and integrity of the ionospheric spatial gradient estimation using an array of GNSS antennas. Our study characterizes the role of contributing factors including number of antennas, number of frequencies, range of frequencies, configuration of the GF antennas, number of satellites, and satellites elevation. Of many detailed studies regarding the ionospheric spatial gradient monitoring techniques, there are quite recent contributions that are also dedicated to the array-based estimation/detection of the ionospheric spatial gradient, see e.g. [7, 11–14]. Our study differs from those contributions in the following four aspects:

1) While multiple baselines are utilized, our approach to the precision and reliability analysis of the ionospheric

spatial gradient remains invariant for the choice of reference antenna, thereby being independent of how receiver pairs are selected to form the baselines, see e.g. [12, 14].

2) Although GBAS is currently operational on a single frequency $L1$, it is going to be modernized to multiple frequencies [15, 16]. Therefore, our analysis is not restricted to the single-frequency GBAS scenario, providing an opportunity to characterize the impact of the number/structure of frequencies on the detection of the ionospheric spatial gradient.

3) In the previous studies, attention is focused on the estimation/detection of the ionospheric spatial gradient based on the observations of a single satellite pair [12–14]. In this study, we relax this assumption by considering the contribution of multiple satellites to the detection of ionospheric spatial gradient. The gradient detection of a single satellite pair would then follow as a special case.

4) We assess how including the observations of more than one epoch contributes to the detection procedure of the ionospheric spatial gradient, for both *ambiguity-float* case and *ambiguity-fixed* case. The impact of the aforementioned contributing factors on integer ambiguity resolution success rate will be investigated as well.

In the present contribution, the precision of the array-based ionospheric spatial gradient estimator will be studied through the analytical structure of its variance matrix, whereas its integrity will be studied by means of its minimal detectable bias (MDB) [17, 18]. The MDBs in this contribution are associated with the uniformly most powerful invariant (UMPI) test [19, 20]. Closed-form expressions of the stated variance matrix and MDBs will be presented as functions of the contributing factors, e.g. number of antennas and number of frequencies. This gives further insights into the role of these contributing factors and allows one to conduct an a-priory analysis before an actual measurement campaign is launched. Our analytical formulation will be accompanied by numerical results.

2 Ionospheric spatial gradient monitoring

2.1 Array-based GNSS model of observations

We assume that the GNSS signals transmitted by m satellites on f frequencies, are tracked by n receivers. If the relative receivers positions and tropospheric delays are known, the multivariate double-differenced (DD) GNSS observation equations can be written in the compact form,

$$E\begin{bmatrix} \underline{p}_R^S \\ \underline{\phi}_R^S \end{bmatrix} = \begin{bmatrix} I_{m-1}\otimes\mu\otimes I_{n-1} & 0 \\ -I_{m-1}\otimes\mu\otimes I_{n-1} & I_{m-1}\otimes\Lambda\otimes I_{n-1} \end{bmatrix}\begin{bmatrix} \iota_R^S \\ z_R^S \end{bmatrix} \quad (1)$$

where $E[.]$ is the expectation operator, and $\otimes$ denotes the Kronecker product [21]. Considering p and q as, respectively, the pivot receiver and the pivot satellite, the DD 'observed-minus-computed' code observations associated with n receivers, satellite s and satellite q on frequency j are stacked in the $(n-1)$-vector $p_{R,j}^{qs} = [p_{p1,j}^{qs},\ldots,p_{pn,j}^{qs}]^T$. The $f(n-1)$-vector $p_R^{qs} = [p_{R,1}^{qs^T},\ldots,p_{R,f}^{qs^T}]^T$ then contains all the DD code observations associated with satellites s and q. The $f(n-1)(m-1)$-vector of the DD code observations is structured as $p_R^S = [p_R^{q1^T},\ldots,p_R^{qm^T}]^T$. The $f(n-1)(m-1)$-vector of phase observations is obtained likewise. The $f(n-1)(m-1)$-vector of integer-valued DD ambiguities z_R^S, in cycles, has the same order as $\underline{p}_R^S/\underline{\phi}_R^S$. ι_R^S is the $(n-1)(m-1)$-vector of the DD first-order ionospheric delays on the first frequency. I_f is the identity matrix of size f. Λ =diag$(\lambda_1,\ldots,\lambda_f)$ with λ_j the wavelength of frequency f_j. The f-vector μ includes the frequency-dependent ratios $\mu_j = \lambda_j^2/\lambda_1^2$.

The stochastic model is assumed given as

$$D\begin{bmatrix} \underline{p}_R^S \\ \underline{\phi}_R^S \end{bmatrix} = \begin{bmatrix} \sigma_p^2 & 0 \\ 0 & \sigma_\phi^2 \end{bmatrix}\otimes D_m^T W^{-1} D_m \otimes I_f \otimes D_n^T D_n \quad (2)$$

where $D[.]$ is the dispersion operator. The $(m-1)\times m$ matrix D_m^T and $(n-1)\times n$ matrix D_n^T are the differencing operators. σ_p and σ_ϕ are, respectively, the zenith-referenced standard deviation of the undifferenced code and phase observables. W =diag$(w^1,\ldots,w^m)$ contains the satellite-elevation-dependent weights w^s. In this paper, we use the following form [22]

$$w^s = [1+10\exp(-\frac{\varepsilon^s}{10^\circ})]^{-2} \quad (3)$$

with ε^s being the elevation of satellite s in degrees. If $\varepsilon^s = 90^\circ$, then w^s is in agreement with 1 up to 2 digits after the decimal point.

Our aim, in this study, is to detect the ionospheric spatial gradient using an array of GNSS antennas. When we speak of an array of antennas, it means that the antennas are located within few kilometers of each other. For such a small-size array, one can make some assumptions leading to a more simplified model of observations to work with. One of the possible suppositions is that signals from a particular GNSS satellite to all the antennas existing in the array experience almost the same ionospheric delays under nominal ionosphere condition (no ionospheric front or storm), leading to the ionospheric delays becoming independent of the receiver location. Under these circumstances, the DD ionospheric delays are zero. Hence, with $\iota_R^S = 0$, our working hypothesis H_o follows then from Eq. (1) as

$$E\begin{bmatrix} \underline{p}_R^S \\ \underline{\phi}_R^S \end{bmatrix}_{H_o} = \begin{bmatrix} 0 \\ I_{m-1}\otimes\Lambda\otimes I_{n-1} \end{bmatrix} z_R^S \quad (4)$$

In the single-epoch case, the number of observations, number of unknowns and the redundancy of the model of observations under H_o are, respectively, $2f(m-1)(n-1)$, $f(m-1)(n-1)$ and $f(m-1)(n-1)$.

In case an ionospheric front affects the signals of one or more satellites, the assumption that the ionospheric delays do not depend on the location of the receivers will not be valid anymore for the contaminated satellites. In previous studies, only the GPS system has been considered, and it is asserted that the probability of a large gradient affecting more than one satellite is sufficiently low, see e.g. [14, 23]. However, when other GNSS systems, e.g. GLONASS and Galileo, are involved, the likelihood of having more than one satellite influenced by the ionospheric front, would increase. Here, in line with previous studies, we consider the case that only one satellite, say c, is contaminated by the ionospheric front.

Many studies have considered that the impact of ionospheric fronts on the GNSS signals changes almost linearly with the distance between two points [8, 24]. Therefore, the ionospheric delay experienced by a signal from satellite c to antenna r in the array can be approximated by its first-order Taylor expansion around an arbitrary point (located within few kilometers with respect to the array) as

$$\imath_r^c \approx \imath_0^c + g^T b_r \tag{5}$$

with b_r being the baseline vector of receiver r with respect to the mentioned arbitrary point, and $\imath_0^c$ being the ionospheric delay on the signal between satellite c and the mentioned arbitrary point. g is the 3-vector of the first-order partial derivative of the ionospheric delay with respect to the receiver position, which is referred to as the *ionospheric spatial gradient*. As mentioned before, ionospheric delays have both spatial and temporal variations. In Eq. (5), the temporal variation has not been modeled. Figure 1 shows the impact of the ionospheric front on the signals of one of the GNSS satellites as function of the between-antennas baseline vector.

In order to see how the ionospheric spatial gradient affects the DD GNSS observables, we start with the undifferenced level. The ionospheric delays on the first frequency associated with n receivers and satellite s are stacked in the n-vector $\tilde{\imath}_R^s = [\tilde{\imath}_1^s, \ldots, \tilde{\imath}_n^s]^T$. The nm-vector of the undifferenced ionospheric delays is structured as $\tilde{\imath}_R^S = [\tilde{\imath}_R^{1^T}, \ldots, \tilde{\imath}_R^{c^T}, \ldots, \tilde{\imath}_R^{m^T}]^T$. Applying the DD operator $D_m^T \otimes D_n^T$ on to the both sides of the last equation, those ionospheric delays associated with the uncontaminated satellites will disappear. Therefore we have

$$\imath_R^S = (D_m^T u_m^c \otimes D_n^T)\tilde{\imath}_R^c \tag{6}$$

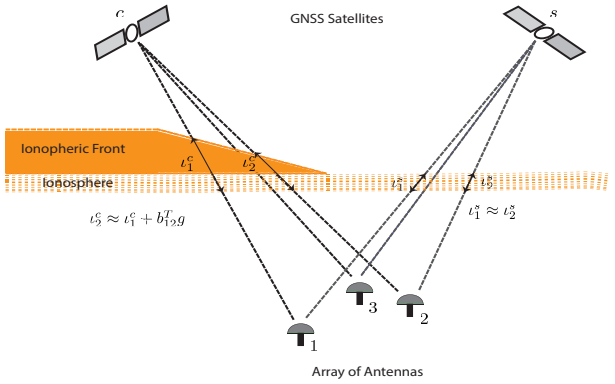

Figure 1. An ionospheric front affects the signals from satellite c to the array of antennas. The ionospheric delays experienced by the signals from satellite s can be considered the same. The ionospheric delays experienced by the signals from satellite c are related to each other through the ionospheric spatial gradient g and the baseline vector between them b_{12}.

in which the m-vector u_m^c is a canonical unit vector with 1 as its c^{th} element and zeros elsewhere. $\tilde{\imath}_R^c$ can be parametrized using Eq. (5) as

$$\tilde{\imath}_R^c = e_n \imath_0^c + B g \tag{7}$$

where the $n \times 3$ matrix B includes the vectors b_r^T $(r = 1, \ldots, n)$ as its rows, and e_n is the n-vector of ones. Combining Eqs. (6) and (7), we get

$$\imath_R^S = (D_m^T u_m^c \otimes D_n^T B) g \tag{8}$$

Since $D_n^T e_n = 0$, $\imath_0^c$ is eliminated in Eq. (8). Substituting Eqs. (8) into (1), we obtain the alternative model H_a as

$$E\begin{bmatrix} \underline{p}_R^S \\ \underline{\phi}_R^S \end{bmatrix}_{H_a} = \begin{bmatrix} D_m^T u_m^c \otimes \mu \otimes D_n^T B & 0 \\ -D_m^T u_m^c \otimes \mu \otimes D_n^T B & I_{m-1} \otimes \Lambda \otimes I_{n-1} \end{bmatrix} \begin{bmatrix} g \\ z_R^S \end{bmatrix} \tag{9}$$

If matrix B satisfies $D_n^T B = 0$, it means that all the antennas are in the same place. The ionospheric spatial gradient will then not be estimable. As a result, the DD observation equations will only contain the DD ambiguities as the unknown parameters, which is desirable for the estimation of the DD ambiguities since only the highly precise phase observables contribute to their estimation and precision. The number of observations, number of unknowns and the redundancy of the model of observations under H_a are, respectively, $2f(m-1)(n-1)$, $f(m-1)(n-1)+l$ and $f(m-1)(n-1)-l$, with l being the dimension of the array (the number of estimable components of the ionospheric spatial gradient).

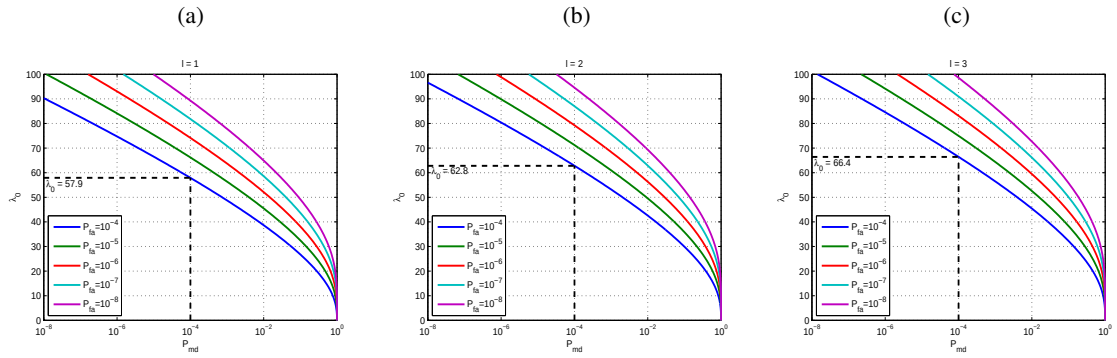

Figure 2. Chi-square non-centrality parameter λ_0 versus probability of missed detection P_{md} for different values of probability of false alarm P_{fa} when the degrees of freedom is (a) $l = 1$; (b) $l = 2$; (c) $l = 3$.

2.2 *Testing procedure*

To detect the ionospheric spatial gradient, we employ the UMPI test [20], as it results in the highest probability of the detection for a class of critical regions. The UMPI test statistic formed to detect and identify the ionospheric bias g reads [20, 25]

$$\underline{T}_l = \underline{\hat{g}}^T Q_{\hat{g}\hat{g}}^{-1} \underline{\hat{g}} \tag{10}$$

where $\underline{\hat{g}}$ and $Q_{\hat{g}\hat{g}}$ are, respectively, the best linear unbiased estimator (BLUE) of g and its corresponding variance matrix, computed under H_a (that is Eq. (9)). The subscript l shows the number of (functions of) estimable components of vector g. If the GNSS phase and code observables are normally distributed, $\underline{\hat{g}}$ as a linear function of them is also normally distributed, i.e. $\underline{\hat{g}} \sim N(g, Q_{\hat{g}\hat{g}})$. The distribution of $\underline{T}_l$ under H_o is then the central Chi-square with l degrees of freedom, i.e. $\underline{T}_l \sim \chi^2(l,0)$, and under H_a the Chi-square with l degrees of freedom and the non-centrality parameter λ, i.e. $\underline{T}_l \sim \chi^2(l,\lambda)$, where $\lambda = g^T Q_{\hat{g}\hat{g}}^{-1} g$. Given the false alarm rate P_{fa}, if $\underline{T}_l > \chi^2_{P_{fa}}(l,0)$, then H_o is rejected in favor of H_a. Here $\chi^2_{P_{fa}}(l,0)$ is the critical value obtained from the distribution $\chi^2(l,0)$ and chosen false alarm rate P_{fa}. The probability of missed detection can be determined by the use of P_{fa}, λ and l [20]. The reverse procedure can also be followed, which means that based on P_{fa}, P_{md} and l, the non-centrality parameter can be computed as $\lambda_0 = \lambda(P_{fa}, P_{md}, l)$ visualized in Figure 2 [17, 20]. For example, when $P_{fa} = 10^{-4}$ and $P_{md} = 10^{-4}$, the non-centrality parameter would be $\lambda_0 = 57.9$, $\lambda_0 = 62.8$ and $\lambda_0 = 66.4$ for, respectively, $l = 1$, $l = 2$ and $l = 3$.

The boundary of the ellipsoidal MDB region is defined as $\lambda_0 = g^T Q_{\hat{g}\hat{g}}^{-1} g$ [20]. Parametrizing the MDB-vector as $g = ||g|| d$, with unit l-vector d, the MDB can be computed as

$$||g|| = \sqrt{\frac{\lambda_0}{d^T Q_{\hat{g}\hat{g}}^{-1} d}} \tag{11}$$

If the unit vector d sweeps the surface of the unit sphere in $\mathbb{R}^l$, the whole MDB region is obtained. The shape and the orientation of the MDB region is governed by $Q_{\hat{g}\hat{g}}$, and its size is determined by λ_0. The MDB region is an interval when $l = 1$, an ellipse when $l = 2$, and an ellipsoid when $l = 3$.

The variance matrix $Q_{\hat{g}\hat{g}}$, and, as a result, the MDB depend on several contributing factors like number of receivers, number of satellites, array configuration etc. Before conducting the actual measurements, one can decide on these contributing factors such that the requirements of the application at hand are satisfied. For instance, civil aviation precision approach needs to detect ionospheric spatial gradient greater than 300 mm/km with the probability of 0.9999 [14, 23, 26].

In the following, we will present analytical expressions for $Q_{\hat{g}\hat{g}}$ and the corresponding MDB. Numerical evidence will also be provided to support closed-form formulas.

3 Ionospheric spatial gradient UMPI MDB

3.1 *Single-epoch ambiguity-float scenario*

To obtain closed-form expressions for $Q_{\hat{g}\hat{g}}$ and the corresponding MDB-vector $||g||d$, we start with the single-epoch ambiguity-float scenario. It can be shown that the variance matrix of the ionospheric spatial gradient estimator and its corresponding MDB, for 3-dimensional, 2-dimensional and 1-dimensional arrays read

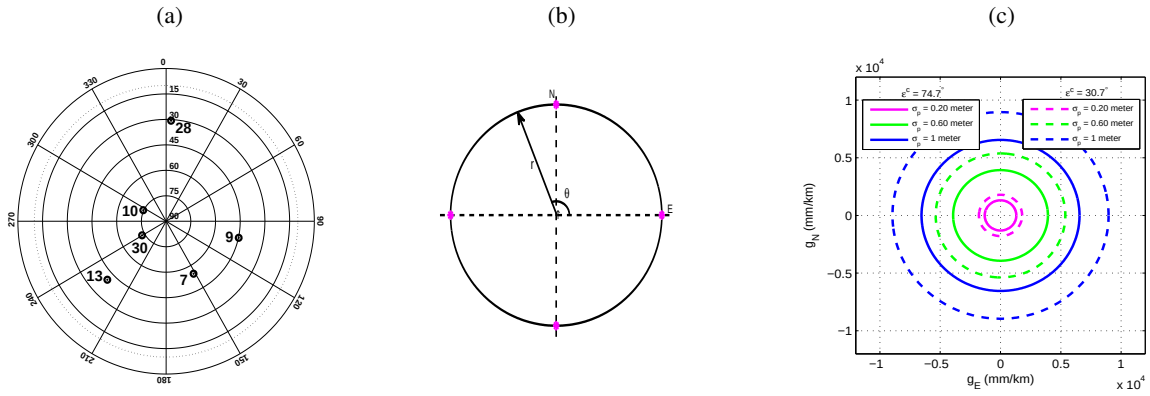

Figure 3. (a) GPS satellites configuration; (b) Positions of the receivers (purple points) in a circular array with the radius of $r = 500$ meter and with the angles $\theta = 0^\circ,\ 90^\circ,\ 180^\circ,\ 270^\circ$; (c) The ellipses showing the corresponding single-epoch ambiguity-float MDBs, with $f = 2$ $(L1 + L2)$, $m = 6$, $n = 4$, $P_{fa} = 10^{-4}$ and $P_{md} = 10^{-4}$ for different values of σ_p. Solid and dashed curves are associated with when, respectively, the highest satellite PRN10 with the elevation $\varepsilon^c = 74.7^\circ$ and the lowest satellite PRN28 with the elevation $\varepsilon^c = 30.7^\circ$ are contaminated by the ionospheric front.

3-dimensional array

$$Q_{\hat{g}\hat{g}} = \frac{\sigma_p^2}{c_f^2 \times c_s^2} \times C_r^{-1} \tag{12}$$

$$||g||_d = \frac{\sigma_p}{c_f \times c_s} \sqrt{\frac{\lambda_0}{d^T C_r d}} d,\ \ d \in \mathbb{R}^3 \tag{13}$$

2-dimensional array

$$Q_{\hat{\tilde{g}}\hat{\tilde{g}}} = \frac{\sigma_p^2}{c_f^2 \times c_s^2} \times \tilde{\tilde{C}}_r^{-1} \tag{14}$$

$$||\tilde{\tilde{g}}||_d = \frac{\sigma_p}{c_f \times c_s} \sqrt{\frac{\lambda_0}{d^T \tilde{\tilde{C}}_r d}} d,\ \ d \in \mathbb{R}^2 \tag{15}$$

1-dimensional array

$$\sigma_{\hat{\tilde{g}}}^2 = \frac{\sigma_p^2}{c_f^2 \times c_s^2} \times \tilde{C}_r^{-1} \tag{16}$$

$$|\tilde{g}| = \frac{\sigma_p}{c_f \times c_s} \sqrt{\frac{\lambda_0}{\tilde{C}_r}} \tag{17}$$

where

$$c_f = \sqrt{f(\bar{\mu}^2 + \sigma_\mu^2)}\ ,\ c_s = \sqrt{w^c (1 - \frac{w^c}{m\overline{w}})} \tag{18}$$

$$C_r = (B - e_n b_{\bar{r}}^T)^T (B - e_n b_{\bar{r}}^T) \tag{19}$$

$$\tilde{\tilde{C}}_r = [u,v]^T C_r [u,v]\ ,\ \tilde{C}_r = [u]^T C_r [u] \tag{20}$$

with $b_{\bar{r}}^T = \frac{1}{n} e_n^T B$, $\bar{\mu} = \frac{1}{f}\sum_{j=1}^{f} \mu_j$, $\sigma_\mu^2 = \frac{1}{f}\sum_{j=1}^{f} (\mu_j - \bar{\mu})^2$, $\overline{w} = \frac{1}{m}\sum_{s=1}^{m} w^s$, and u, v forming an orthonormal basis of the array-plane such that u spans the linear array. $||\tilde{\tilde{g}}||$ is the norm of the projection of g onto the array-plane spanned by u, v, and $|\tilde{g}|$ is the absolute value of the projection of g onto the linear-array spanned by u. Be aware that the ionospheric spatial gradient component(s) orthogonal to the array is (are) not estimable.

Eq. (19) shows that both the variance matrix and the corresponding MDBs are invariant for our choice of the reference receiver, and hence how receiver pairs are selected to form the baselines. From Eqs. (12), (14) and (16), we do see that the precision of the ionospheric spatial gradient is dominated by code observables. That is because in single-epoch ambiguity-float scenario, all the DD phase observables are preserved for the DD ambiguities. Therefore, the estimator of the ionospheric spatial gradient, the so-called *float-solution*, does not benefit from the high phase precision.

The main difference between the MDB regions of different types of arrays lies in λ_0 (because of different values for l) and the array configuration. Based on the analytical expressions derived above, we conduct a pre-analysis on the role played by various contributing factors in the MDB region of ionospheric spatial gradient. All the conclusions are valid for all types of arrays. We also present our conclusions visually for a planar array, which can also be illustrated for other types of arrays in a similar way. Only for simplicity, we consider a circle to put antennas over and make use of polar coordinates with respect to its center.

Code-precision-specific contribution: There is a direct relation between the MDB and σ_p, such that an increment in σ_p will result in MDB region growing. Figure 3 depicts the impact of σ_p on the MDB region, for the shown planar array and satellite geometry. The coordinates of antennas with respect to the center of circle have the form of $b_r = [r\cos\theta\ ,\ r\sin\theta]^T$. Since the geometry of the array is symmetric, the MDB region would be of circle shape. The use is made of frequencies $L1$ and $L2$. P_{fa} and P_{md} should be set based on the requirements of the specific application at hand. For civil aviation applications, '*however, a standardized way of determining such a probability has not yet been developed and needs to be investigated*' [23]. Here, we choose $P_{fa} = 10^{-4}$ and $P_{md} = 10^{-4}$, consistent with the previous works [13, 14, 27]. The graphs in this figure have been plotted for two extreme cases, namely the signals from the highest PRN10 and the lowest PRN28 satellites are contaminated by the ionospheric front. The linear dependency between the MDB size and σ_p is visible in this figure.

g_E and g_N in Figure 3 (and all the figures coming after) are, respectively, the projection of g on the East and North direction.

Non-centrality-specific contribution: The MDB is proportional to the square-root of λ_0. From Figure 2, for a given P_{fa}, λ_0 will get higher values for smaller P_{md} and larger p. Larger λ_0 would result in larger MDBs.

Satellite-specific contribution: GNSS satellites effect has three aspects, which are number of satellites m, satellites elevation through the mean elevation-dependent weight $\overline{w}$, and elevation of the contaminated satellite through the elevation-dependent weight w^c. Assuming that $w^1 \approx \ldots \approx w^m \approx \overline{w}$, it can be seen that the number of satellites affects the MDB by approximately $\sqrt{m/(m-1)}$. Since the growth speed of $\sqrt{m/(m-1)}$ is much less than that of m, the rate of change of MDB as function of number of satellites will not be very considerable after adding a particular number of satellites. Figure 4 shows the behavior of MDB for different numbers of satellites, for the planar array and satellite geometry in Figure 3. The MDB region experiences a notable decrease when going from $m = 2$ to $m = 4$. As more other satellites are included, the improvement of MDB decreases.

Satellite elevations manifest themselves through the elevation-weighting $\overline{w}, w^c$, which are reversely related to the satellite elevation. Two questions may be asked here: 1) what is the best constellation to detect ionospheric spatial gradient? 2) given a specific constellation, on which satellite, ionospheric spatial gradient can be detected the best? To answer the first question, we consider the follow-

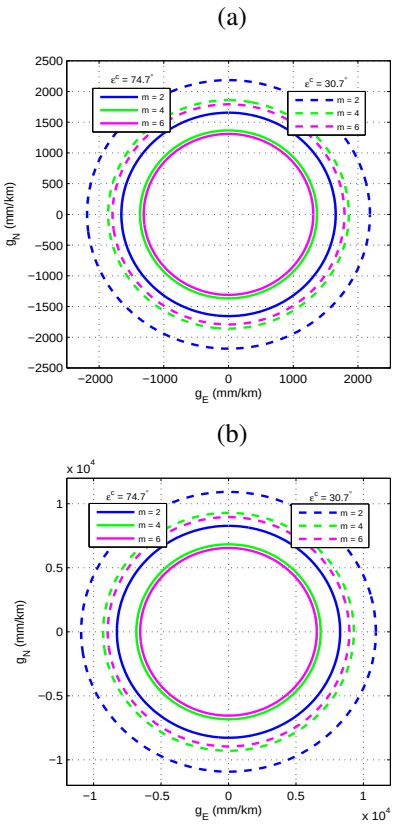

Figure 4. The single-epoch ambiguity-float MDBs corresponding with the planar array and satellite geometry in Figure 3, with $f = 2$ ($L1 + L2$), $n = 4$, $P_{fa} = 10^{-4}$ and $P_{md} = 10^{-4}$ for different values of m and (a) $\sigma_p = 0.2$ meter; (b) $\sigma_p = 1$ meter. For plotting solid and dashed curves, satellites are, respectively, sorted in a descending and ascending order in terms of their elevations. Then, we start from first 2 satellites and add more other ones. For each ordering, the first satellite is considered to be contaminated by the ionospheric front, for descending order the highest satellite PRN10 with the elevation $\varepsilon^c = 74.7°$ and for ascending order the lowest satellite PRN28 with the elevation $\varepsilon^c = 30.7°$.

ing equivalent expression for c_s

$$c_s = \left(\frac{1}{w^c} + \frac{1}{\sum_{s=1,s\neq c}^{m} w^s}\right)^{-\frac{1}{2}} \tag{21}$$

based on which, one can easily conclude that the maximum value for c_s is obtained when all the visible satellites are in zenith, i.e. $\varepsilon^s = 90°$ ($s = 1,\ldots,m$). Therefore, the best satellite configuration in terms of ionospheric spatial gradient detectability is the one containing zenith-elevated satellites.

When it comes to the second question, $m\overline{w}$ in c_s formula-

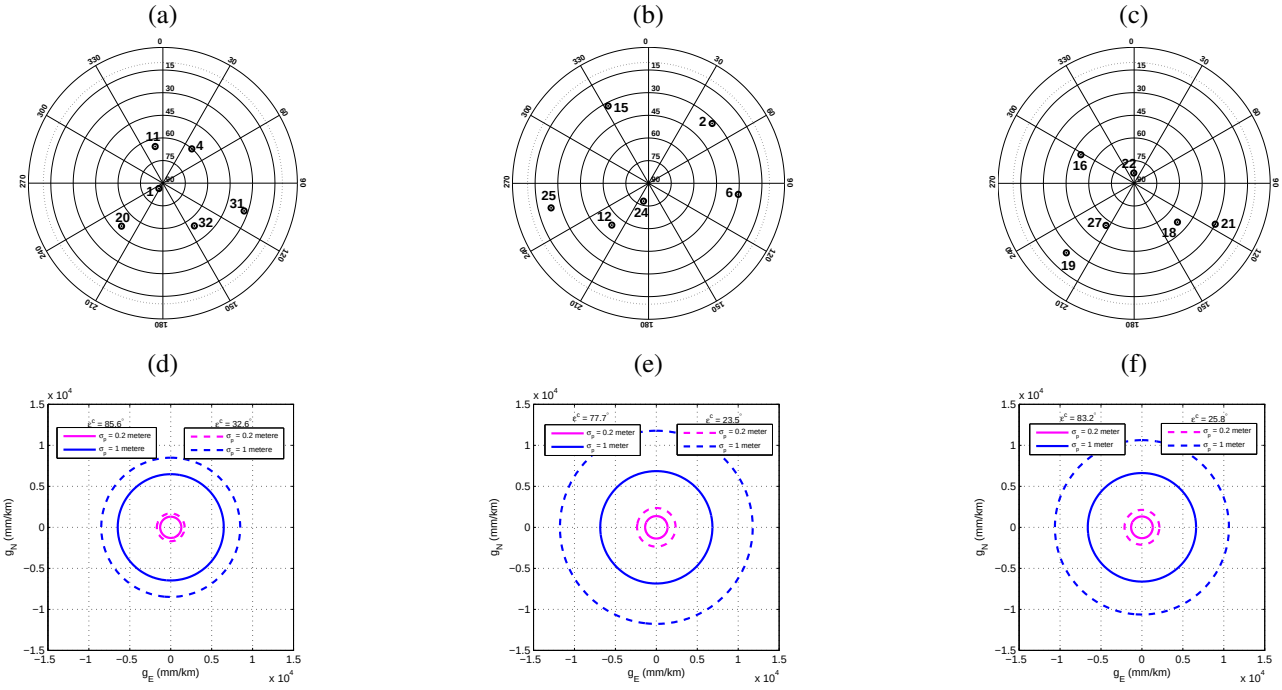

Figure 5. GPS satellites configurations where (a) most of the satellites have almost high elevations; (b) most of the satellites have low elevations; (c) some of the satellites have high elevations and some low elevations. The ellipses showing the single-epoch ambiguity-float MDBs corresponding with the planar array in Figure 3 and (d) satellite configuration in (a); (e) satellite configuration in (b); (e) satellite configuration in (c), with $f = 2$ $(L1+L2)$, $m = 6$, $n = 4$, $P_{fa} = 10^{-4}$ and $P_{md} = 10^{-4}$. Solid and dashed curves are associated with when, respectively, the highest satellites, PRN1 with the elevation $\varepsilon^c = 85.6°$ in (a), PRN24 with the elevation $\varepsilon^c = 77.7°$ in (b), PRN22 with the elevation $\varepsilon^c = 83.2°$ in (c), and the lowest satellites, PRN31 with the elevation $\varepsilon^c = 32.6°$ in (a), PRN25 with the elevation $\varepsilon^c = 23.5°$ in (b), PRN19 with the elevation $\varepsilon^c = 25.8°$ in (c), are contaminated by the ionospheric front.

tion is constant. In that case, the behavior of c_s with respect to changes in w^c is parabolic. It can be shown that c_s reaches its maximum value when $w^c = \sum_{s=1,s\neq c}^{m} w^s$. Therefore, the best detectability of the ionospheric spatial gradient would be realized when the ionospheric front affects, among the satellites in view, that satellite of which the elevation-dependent weight is the closest to $\sum_{s=1,s\neq c}^{m} w^s$. The worst detectability is associated with those satellites of which the elevation-dependent weights are the furthest from $\sum_{s=1,s\neq c}^{m} w^s$.

Figure 5 illustrates 3 GPS satellite configurations when (a) most of the satellites have almost high elevations, (b) most of the satellites have almost low elevations, (c) some of the satellites have high elevations and some low elevations. Table 1 shows the values of $\frac{w^c}{\sum_{s=1,s\neq c}^{m} w^s}$ and c_s for these configurations when the lowest and highest satellites are contaminated. We can see that within each satellite configuration, $\frac{w^c}{\sum_{s=1,s\neq c}^{m} w^s}$ gets its largest value when the highest satellite is corrupted by the ionospheric front. Moreover, the higher the elevations of the satellites in view, the better the ionospheric spatial gradient would be detectable.

Frequency-specific contribution: Three parameters represent the influence of the GNSS signal frequencies on the MDB, which are number of frequencies f, squared mean of the frequencies ratios $\bar{\mu}^2$, and the dispersion of the frequencies ratios σ_μ^2. The more frequencies are used, the MDB region will decrease more. If we go from single-frequency $(L1)$ to dual-frequency $(L1+L2)$ model of observations, then $\bar{\mu}^2$ increases from 1 to almost 1.7, and σ_μ^2 grows from 0 to almost 1. Therefore, the MDB region corresponding with the dual-frequency scenario is nearly 2 times smaller than that corresponding with the single-frequency scenario. It is shown in Figure 6.

Array-specific contribution: The contribution of the array is characterized through the number of receivers n and the array configuration B. As the number of receivers increases, the MDB region gets smaller in all or some particular directions depending on the array geometry. Figure 7 illustrates the MDB regions as function of number of receivers for the satellite geometry in Figure 3. When

Table 1. The values of $\frac{w^c}{\sum_{s=1,s\neq c}^{m} w^s}$ and c_s for the satellite configurations in Figure 5.

	Satellite configuration (a)		Satellite configuration (b)		Satellite configuration (c)	
	PRN1	PRN31	PRN24	PRN25	PRN22	PRN19
$\frac{w^c}{\sum_{s=1,s\neq c}^{m} w^s}$	0.234	0.110	0.375	0.078	0.287	0.078
c_s	0.898	0.685	0.849	0.494	0.879	0.547

the green receiver is added to the existing 4 blue receivers in the North-East direction, the detectability in the same direction improves. The change of MDB region due to including other receivers can be interpreted likewise.

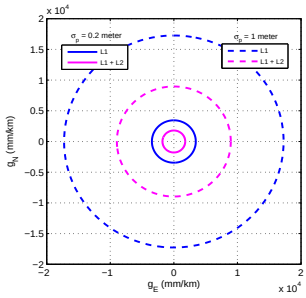

Figure 6. The ellipses showing the single-epoch ambiguity-float MDBs corresponding with the planar array and satellite geometry in Figure 3, with $m = 6$, $n = 4$, $P_{fa} = 10^{-4}$ and $P_{md} = 10^{-4}$ for different number of frequencies. Solid and dashed curves are, respectively, associated with $\sigma_p = 0.2$ meter and $\sigma_p = 1$ meter. The lowest satellite PRN28 with the elevation $\varepsilon^c = 30.7^\circ$ has been considered to be contaminated by the ionospheric front.

If the length of the array increases, then the term C_r^{-1} decreases, so does the MDB region. In Figure 8, the MDB region has been plotted for different lengths of array for the array configuration and satellite geometry in Figure 3. An equivalent form for C_r^{-1} can be obtained as

$$C_r^{-1} = (B^T B)^{-1} + \frac{(B^T B)^{-1} B^T e_n e_n^T B (B^T B)^{-1}}{n - e_n^T P_B e_n} \qquad (22)$$

with $P_B = B(B^T B)^{-1} B^T$. The smaller $e_n^T B$ (the projection of matrix B onto the vector e_n), the smaller C_r^{-1}. If $e_n^T B = 0$, then the second term in Eq. (22) will disappear. A symmetric array geometry satisfies $e_n^T B = 0$, hence being desirable in terms of the MDB region size. The vector e_n is the orthogonal complement of the space formed by the columns of differencing matrix D_n, i.e. $D_n^T e_n = 0$.

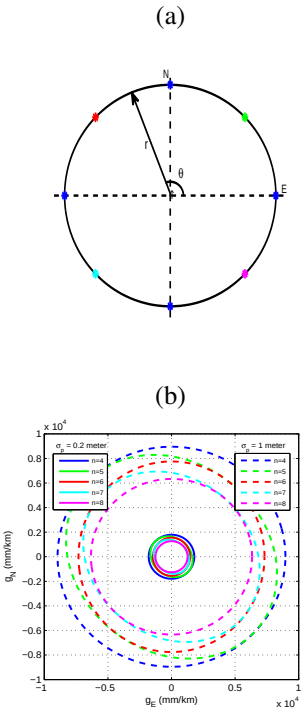

Figure 7. (a) Positions of the receivers (colored points) in a circular array with the radius of $r = 500$ meter and with the angles $\theta = 0^\circ, 45^\circ, 90^\circ, 135^\circ, 180^\circ, 225^\circ, 270^\circ, 315^\circ$; (b) The ellipses showing the single-epoch ambiguity-float MDBs corresponding with the satellite geometry in Figure 3 and for 4 blue receivers (*blue*), 5 blue+green receivers (*green*), 6 blue+green+red receivers (*red*), 7 blue+green+red+cyan receivers (*cyan*), and 8 blue+green+red+cyan+purple receivers (*purple*), with $f = 2$ $(L1 + L2)$, $m = 6$, $P_{fa} = 10^{-4}$ and $P_{md} = 10^{-4}$. Solid and dashed curves are, respectively, associated with $\sigma_p = 0.2$ meter and $\sigma_p = 1$ meter. The lowest satellite PRN28 with the elevation $\varepsilon^c = 30.7^\circ$ has been considered to be contaminated by the ionospheric front.

Therefore, the smaller $D_n^T B$ (the projection of matrix B

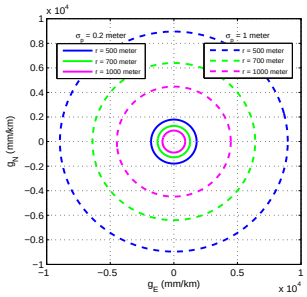

Figure 8. The ellipses showing the single-epoch ambiguity-float MDBs corresponding with the planar array and the satellite geometry in Figure 3, with $f = 2$ $(L1 + L2)$, $m = 6$, $n = 4$, $P_{fa} = 10^{-4}$ and $P_{md} = 10^{-4}$ for various lengths of the array. Solid and dashed curves are, respectively, associated with $\sigma_p = 0.2$ meter and $\sigma_p = 1$ meter. The lowest satellite PRN28 with the elevation $\varepsilon^c = 30.7^\circ$ has been considered to be contaminated by the ionospheric front.

onto the range space of D_n), the larger $e_n^T B$, and the larger C_r^{-1}. The term $D_n^T B$ gets its small values when the baseline vectors b_r $(r = 1, \ldots, n)$ are close to each other. In Figure 9, the MDB regions for different geometries of 4 antennas, and the satellite configuration in Figure 3 are illustrated. In Figure 9 (b), the shape of antennas is almost aligned with the East direction, which is why the corresponding ionospheric spatial gradient MDB ellipse has its minor axis parallel to the East direction. In fact, this shape of array enables the user to find smaller gradients in East direction. The MDB area associated with Figure 9 (c) can be interpreted analogously.

From Figures 3 to 9, it can be seen that achieving small MDBs for the ionospheric spatial gradient with test in Eq. (10) with $P_{fa} = 10^{-4}$ and $P_{md} = 10^{-4}$ based on the single-epoch code observables (ambiguity-float scenario) would require a large number of receivers or long distances between antennas. The above MDBs might be desirable for some special applications, but not for civil aviation precision approach. For such an application, due to the airport geometry and the high price of the receivers, increasing the number of receivers or the length of the array may not always be possible. So, does it mean it is impossible to detect ionospheric spatial gradient at the level of 300 mm/km upon the single-epoch observations? We answer this question in the following.

3.2 Single-epoch ambiguity-fixed scenario

Once the DD ambiguities are fixed, the phase observables would also contribute to the estimation of the ionospheric spatial gradient, hence improving its precision and reducing the MDB region size. The variance matrix of the ionospheric spatial gradient estimator after fixing the DD ambiguities, the so-called *fixed solution*, and the corresponding MDB can be shown to have the following form for the 3-dimensional array

$$Q_{\check{g}\check{g}} = \frac{\varepsilon}{1+\varepsilon} Q_{\hat{g}\hat{g}} \tag{23}$$

$$||g||d = \sqrt{\frac{\varepsilon}{1+\varepsilon}} \left[\frac{\sigma_p}{c_f \times c_s} \sqrt{\frac{\lambda_0}{d^T C_r d}} d\right],\ d \in \mathbb{R}^3 \tag{24}$$

where $\varepsilon = \sigma_\phi^2 / \sigma_p^2 \approx 10^{-4}$. For other types of array, the same relationship between float and fixed parameters holds true. Comparing Eqs. (23)/(24) and (12)/(13), if one can fix the DD ambiguities successfully at a single epoch, then the precision of ionospheric spatial gradient estimator improves by 10^4, and the size of the corresponding MDB region reduces by 10^2. Therefore, it is important to know how it would be possible to fix the DD ambiguities with an acceptable success rate at only one epoch. The success rate of the integer DD ambiguity resolution depends on their variance matrix. It can be shown that the variance matrix of the DD ambiguities for single-epoch scenario based on Eqs. (9) (fault-affected model H_a) and (2) reads

$$\begin{aligned} Q_{\hat{z}_R^S \hat{z}_R^S} &= \underbrace{\sigma_\phi^2 D_m^T W^{-1} D_m \otimes \Lambda^{-2} \otimes D_n^T D_n}_{C_\phi} \\ &\quad + \underbrace{D_m^T u_m^c u_m^{c\,T} D_m \otimes \Lambda^{-1} \mu \mu^T \Lambda^{-1} \otimes D_n^T B Q_{\hat{g}\hat{g}} B^T D_n}_{C_p} \end{aligned} \tag{25}$$

This variance matrix of order $f(m-1)(n-1)$ has two terms. The first term C_ϕ is dominated by high phase precision, while the second one C_p is dominated by poor code precision. C_p is due to the presence of the ionospheric spatial gradient in model H_a. In other words, based on the model of observations in Eq. (4) (fault-free model H_o), C_p would disappear. In that case, the precision of the DD ambiguities would be at the level of the DD phase precision.

Based on Eq. (25), we can analyze the efficacy of various factors on the precision of the DD ambiguities estimators and the consequent integer ambiguity resolution success rate. But, since the only purpose of fixing the ambiguities is to improve the precision of the ionospheric spatial gradient, it is important to know how setting these factors in favor of the ambiguity resolution, affects the variance matrix of the fixed ionospheric spatial gradient estimator $Q_{\check{g}\check{g}}$.

Looking at Eqs. (23) and (25), $Q_{\hat{z}_R^S \hat{z}_R^S}$ and $Q_{\check{g}\check{g}}$ are both dependent on $Q_{\hat{g}\hat{g}}$. The variance matrix of the fixed solution $Q_{\check{g}\check{g}}$ is a ratio of that of the float solution $Q_{\hat{g}\hat{g}}$, and

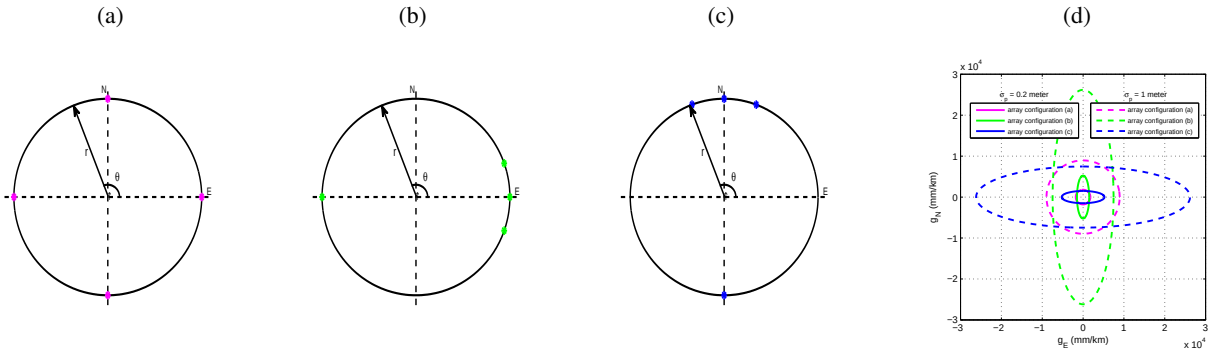

Figure 9. Positions of the receivers (colored points) in a circular array with the radius of $r = 500$ meter and with the angles (a) $\theta = 0^\circ, 90^\circ, 180^\circ, 270^\circ$; (b) $\theta = 0^\circ, 20^\circ, 180^\circ, 340^\circ$; (c) $\theta = 70^\circ, 90^\circ, 110^\circ, 270^\circ$; (d) The ellipses showing the single-epoch ambiguity-float MDBs corresponding with the planar arrays in (a), (b) and (c) and the satellite geometry in Figure 3, with $f = 2$ $(L1 + L2)$, $m = 6$, $n = 4$, $P_{fa} = 10^{-4}$ and $P_{md} = 10^{-4}$. Solid and dashed curves are, respectively, associated with $\sigma_p = 0.2$ meter and $\sigma_p = 1$ meter. The lowest satellite PRN28 with the elevation $\varepsilon^c = 30.7^\circ$ has been considered to be contaminated by the ionospheric front.

therefore all the influencing factors mentioned in Subsection 3.1 have the same impact on both of them. $Q_{\hat{z}^S_R \hat{z}^S_R}$ like $Q_{\hat{g}\hat{g}}$ will also benefit from increasing the number of frequencies, and number of satellites. If the ionospheric front contaminates those satellites of which the elevation-dependent weights are near to $\sum_{s=1, s\neq c}^{m} w^s$, then $Q_{\hat{g}\hat{g}}$ and, consequently, $Q_{\hat{z}^S_R \hat{z}^S_R}$ would improve.

If in Eq. (25) we expand $Q_{\hat{g}\hat{g}}$, we will see that the array configuration (B and n) affects $Q_{\hat{z}^S_R \hat{z}^S_R}$ through the term $D_n^T B C_r^{-1} B^T D_n$, which can be extended as

$$D_n^T B C_r^{-1} B^T D_n = D_n^T P_B D_n + \frac{(D_n^T P_B e_n)(D_n^T P_B e_n)^T}{n - e_n^T P_B e_n} \quad (26)$$

Comparing Eqs. (22) and (26), the first observation is that in contrast to $Q_{\check{g}\check{g}}$, $Q_{\check{z}^S_R \check{z}^S_R}$ is independent of the total length of the array. It means that if the receivers positions in the array are all scaled by the same factor, it would have no result on the precision of the DD ambiguities. The second observation is that if $e_n^T B = 0$, the second term in Eq. (26) will disappear. If the design of the array is such that $D_n^T B \to 0$ (b_r's are close to each other), Eq. (26) will get very small values, but the second term in Eq. (22), as was previously described, will get its large values. However, because of the very small value of $\varepsilon = 10^{-4}$ in the formulation of $Q_{\check{g}\check{g}}$, designing the array geometry to the benefit of ambiguity resolution ($D_n^T B \to 0$), should not be an obstacle to achieve the desirable values for the precision of $\check{g}$ and the size of the corresponding MDB.

Table 2 lists the integer least-squares (ILS) [28, 29] success rate, for the satellite configurations in Figure 5 and the illustrated array configurations, for different number of frequencies and different elevations of the contaminated satellite when $\sigma_p = 0.2$ meter. It can be seen when the GNSS observations are made on 2 frequencies ($L1 + L2$), the DD ambiguities can be fixed by 100% regardless of array and satellite configuration, if the elevation of the contaminated satellite is sufficiently high. When the elevation of the contaminated satellite is low, then both array and satellite configurations become important. If the GNSS observations are available on only 1 frequency ($L1$), it is impossible to fix the ambiguities successfully at a single epoch.

Figure (10) (a) and (b) shows MDB regions corresponding to array configurations (2) and (1) in Table 2, respectively, for dual-frequency ambiguity-float scenario. MDB region associated with the array configuration (1) is indeed better than the one corresponding to the array configuration (2), since it is symmetric and its maximum boundary is 10 times smaller. Based on the results in Table 2, it is possible to fix the DD ambiguities associated with the array configuration (2) and satellite configuration (a) at one epoch. Figure (10) (c) illustrates the fixed MDB region. Although it is not symmetric, its maximum boundary is 10 times smaller than that of the float MDB region associated with the array configuration (1). This figure tells us , for some special satellite geometries, it is possible to detect the ionospheric spatial gradient even smaller than 300 mm/km at one single epoch when the shape of the array is to the benefit of the successful ambiguity resolution and the GNSS observables are available on 2 frequencies. For other satellite geometries that the high success rates are not achievable at one epoch, only a few number of epochs are needed to reach a desirable success rate.

Table 2. DD ambiguity resolution ILS success rate $Ps\ (\%)$ as function of the satellite configurations in Figure 5 and the array configurations shown, number of frequencies f, and the elevation of the contaminated satellite ε^c for $\sigma_p = 0.2$ meter.

	Array configuration	ε^c		Satellite configuration (a)		Satellite configuration (b)		Satellite configuration (c)	
				$f=1$	$f=2$	$f=1$	$f=2$	$f=1$	$f=2$
(1)	$r = 500$ meter $\theta = 0°,\ 90°,\ 180°,\ 270°$	Highest	$Ps\ (\%)$	10.921	**100**	9.962	99.999	10.737	**100**
	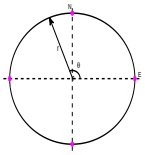	Lowest	$Ps\ (\%)$	6.511	99.926	3.383	97.427	4.289	98.964
(2)	$r = 500$ meter $\theta = 0°,\ 10°,\ 20°,\ 70°$	Highest	$Ps\ (\%)$	65.660	**100**	61.135	**100**	64.325	**100**
	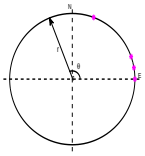	Lowest	$Ps\ (\%)$	44.210	**100**	22.724	99.907	28.058	99.978

Table 3. DD ambiguity resolution ILS success rate $Ps\ (\%)$ as function of the satellite configurations in Figure 5 and the array configurations shown, and the elevation of the contaminated satellite ε^c for $f = 2\ (L1 + L2)$ and $\sigma_p = 1$ meter.

	Array configuration	ε^c		Satellite configuration (a)	Satellite configuration (b)	Satellite configuration (c)
(1)	$r = 500$ meter $\theta = 0°,\ 90°,\ 180°,\ 270°$	Highest	Ps (%)	20.014	16.903	18.836
	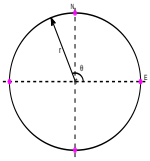	Lowest	Ps (%)	8.689	2.619	3.870
(2)	$r = 500$ meter $\theta = 0°,\ 10°,\ 20°,\ 70°$	Highest	Ps (%)	50.578	44.726	48.171
	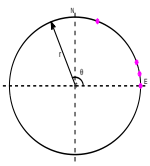	Lowest	Ps (%)	23.83	6.471	10.142

Table 3 contains the ILS success rate for the satellite configurations in Figure 5 and the illustrated array configurations, for $f = 2\ (L1 + L2)$ and different elevations of the contaminated satellite when $\sigma_p = 1$ meter. It shows that for such a large value of σ_p, it would be impossible to reach high values for ILS success rate even if the GNSS observables are available on 2 frequencies.

Up to now, we have assessed the case of detecting iono-

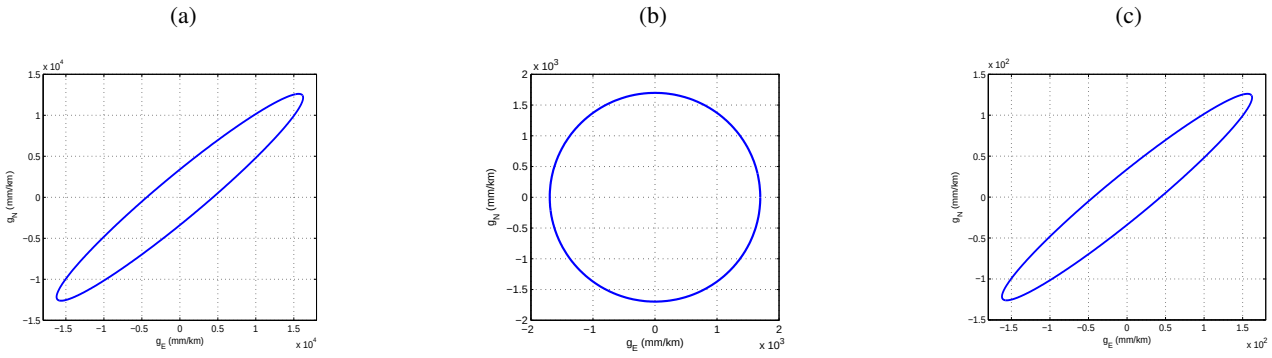

Figure 10. The ellipses showing the (a) single-epoch ambiguity-float MDB corresponding with the planar array (2) in Table 2, (b) single-epoch ambiguity-float MDB corresponding with the planar array (1) in Table 2, (c) single-epoch ambiguity-fixed MDB corresponding with the planar array (2) in Table 2, and the satellite geometry in Figure 5 (a), $f = 2$ $(L1 + L2)$, $m = 6$, $n = 4$, $P_{fa} = 10^{-4}$ and $P_{md} = 10^{-4}$. The lowest satellite PRN31 with the elevation $\varepsilon^c = 32.6^\circ$ has been considered to be contaminated by the ionospheric front.

spheric spatial gradient upon the single-epoch GNSS observables. From the results we obtained above, fixing the DD ambiguities for single-epoch scenario to achieve the desirable MDB regions depends on some factors like the satellite geometry and the elevation of the contaminated satellite which are uncontrollable and probably hinder having acceptable DD ambiguity resolution success rate. It is also known that, since the ambiguities are considered constant over time, if we let the time go on and collect GNSS observables over a particular number of epochs, more precise estimations for the DD ambiguities will be obtained, giving rise to larger success rates. In the following subsection we will address the multi-epoch scenario.

3.3 Multi-epoch scenario

When it comes to multi-epoch scenario, one can think of two cases: 1) ionospheric spatial gradient is time-invariant; 2) ionospheric spatial gradient is time-variant. In Table 4, the variance matrices of the ionospheric spatial gradient estimator corresponding with epoch i are illustrated as function of $Q_{\hat{g}\hat{g}}$ in Eq. (12) specified for epoch i, for several scenarios and the two cases time-invariant and time-variant ionospheric spatial gradient. The closed-form formulations for the MDB can be easily found by substituting the variance matrices into Eq. (11). Although the variance matrix notation in this table is the one used for the 3-dimensional array, the results in this table holds true for all types of array.

Table 4. Variance matrix of the ionospheric spatial gradient vector corresponding with epoch i (ε is the phase-code variance ratio).

Scenario	Iono. gradient	Ambiguity	Variance matrix
Single-epoch	-	float	$Q_{\hat{g}\hat{g}}(i)$
Single-epoch	-	fixed	$\frac{\varepsilon}{1+\varepsilon} Q_{\hat{g}\hat{g}}(i)$
multi-epoch	time-invariant	float	$[\sum_{h=1}^{k} Q_{\hat{g}\hat{g}}^{-1}(h)]^{-1}$
multi-epoch	time-invariant	fixed	$\frac{\varepsilon}{1+\varepsilon}[\sum_{h=1}^{k} Q_{\hat{g}\hat{g}}^{-1}(h)]^{-1}$
multi-epoch	time-variant	float	$\frac{\varepsilon}{1+\varepsilon}(1+\frac{1}{k\varepsilon})Q_{\hat{g}\hat{g}}(i)$
multi-epoch	time-variant	fixed	$\frac{\varepsilon}{1+\varepsilon} Q_{\hat{g}\hat{g}}(i)$

3.3.1 Time-invariant ionospheric spatial gradient

First we consider the case when the ionospheric spatial gradient is time-invariant. When the ambiguities are still float, including the observations of more than one epoch, say k epochs, improves the variance matrix of $\hat{g}$ by almost k factor, and the MDB region by $\sqrt{k}$. Phase observables have no contribution to the variance matrix of $\hat{g}$ unless the integer DD ambiguities are successfully fixed. The reason for this can be explained as follows. We have assumed that both g and z_R^S are constant over time. Therefore, the *time-averaged* DD phase observations are reserved for the integer-valued DD ambiguities, and only the *time-differenced* DD phase observations remain to contribute to the solution of the ionospheric spatial gradient. This contribution would, however, be zero since the *time-differenced* design matrix of the ionospheric spatial gradient is zero, and also phase observables are uncorrelated with the code ones. When the ambiguities are fixed, DD phase observables act as if they are highly precise DD code observables. Hence, both phase and code observables would contribute to the estimation and the corre-

Table 5. Number of epochs needed for the DD ambiguity resolution ILS success rate to reach 99.9999%, as function of the satellite configurations and the array configurations shown, for $f = 2$ $(L1 + L2)$ and $\sigma_p = 1$ meter. The data sampling-rate is 30 seconds.

	Array configuration	ε^c	Ionospheric spatial gradient	Satellite configuration (a)	Satellite configuration (b)	Satellite configuration (c)
(1)	$r = 500$ meter $\theta = 0°,\ 90°,\ 180°,\ 270°$	Highest	time-invariant	24	28	24
			time-variant	23	29	25
	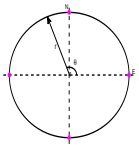	Lowest	time-invariant	44	55	44
			time-variant	43	54	45
(2)	$r = 500$ meter $\theta = 0°,\ 10°,\ 20°,\ 70°$	Highest	time-invariant	14	16	17
			time-variant	13	15	15
	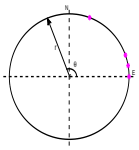	Lowest	time-invariant	25	39	29
			time-variant	25	37	29

sponding variance matrix of the ionospheric spatial gradient. Therefore, the variance matrix of the ionospheric spatial gradient and its associated MDB region will decrease by, respectively, ε and $\sqrt{\varepsilon}$ compared to when the ambiguities are float.

The precision of the DD ambiguities would benefit from the number of epochs. It can be shown that the variance matrix of the DD ambiguities after k epochs has the following form

$$\begin{aligned} Q_{\hat{z}^S_R \hat{z}^S_R} &= \sigma_\phi^2 [\textstyle\sum_{i=1}^k (D_m^T W^{-1}(i) D_m)^{-1}]^{-1} \otimes \Lambda^{-2} \otimes D_n^T D_n \\ &\quad + D_m^T u_m^c u_m^{c\,T} D_m \otimes \Lambda^{-1} \mu \mu^T \Lambda^{-1} \otimes D_n^T B [\textstyle\sum_{i=1}^k Q^{-1}_{\hat{g}\hat{g}}(i)]^{-1} B^T D_n \end{aligned} \tag{27}$$

This shows that $Q_{\hat{z}^S_R \hat{z}^S_R}$ will improve by almost k factor after k epochs. This means that if the values of some uncontrollable factors such as satellites configuration and the number of satellites does not provide us with the required single-epoch precision for the DD ambiguities, then letting the time go on would be of help in that sense.

From Table 3, we saw that when $\sigma_p = 1$ meter, it is impossible to reach high ILS success rates for the ambiguity resolution based on single-epoch observables. In Table 5, one can see the number of epochs (with the sampling-rate of 30 seconds) needed for $Ps = 99.9999\%$ when the ionospheric spatial gradient is time-invariant, for the satellite configurations in Figure 5 and the illustrated array configurations, for $f = 2$ $(L1 + L2)$ and different elevations of the contaminated satellite when $\sigma_p = 1$ meter.

3.3.2 *Time-variant ionospheric spatial gradient*

Now we consider the case where the ionospheric spatial gradient is assumed to change over time. In order to derive closed-form expressions for this case, we have made the assumption that over a limited number of epochs, say k, $w^s(1) \approx \ldots \approx w^s(k) \approx w^s$. The variance matrix of $\hat{g}(i)$ will not be improved by including other epochs observables, in case only code observables are taken into account. That is because, according to Eq. (9), the ionospheric spatial gradient vectors are estimated based on the time-uncorrelated DD code observables and observation models with no common parameters. When the phase observables are also included and the ambiguities are float, the variance matrix of the ionospheric spatial gradient and the corresponding MDB drops by k and $\sqrt{k}$, respectively. When the ambiguities are successfully fixed, DD phase observables act as highly precise DD code observables. In this case, the ionospheric spatial gradient vectors are estimated based on the time-uncorrelated code and phase observables and observation models with no common parameters. So, there would be no correlation among the estimators of the ionospheric spatial gradient associated with various epochs.

Assuming that $w^s(1) \approx \ldots \approx w^s(k) \approx w^s$, the variance matrix of the DD ambiguities after k epochs can be approxi-

mated by

$$Q_{\hat{z}_R^S \hat{z}_R^S} \approx \frac{\sigma_\phi^2}{k} D_m^T W^{-1} D_m \otimes \Lambda^{-2} \otimes D_n^T D_n + \frac{1}{k} D_m^T u_m^c u_m^{c\,T} D_m \otimes \Lambda^{-1} \mu\mu^T \Lambda^{-1} \otimes D_n^T B Q_{\hat{g}\hat{g}}(i) B^T D_n \quad (28)$$

which clearly shows $Q_{\hat{z}_R^S \hat{z}_R^S}$ will decrease by almost k after k epochs.

Table 5 shows the number of epochs needed for the DD ambiguity resolution ILS success rate to reach $Ps = 99.9999\%$ when the ionospheric spatial gradient is time-variant, for $f = 2$ $(L1 + L2)$ and $\sigma_p = 1$ meter, as function of the array configurations, the satellite configurations, and the elevation of the contaminated satellite.

According to Table 5, fixing the DD ambiguities does not have a dependency on whether the ionospheric spatial gradient is time-invariant or time-variant. This conclusion has already been confirmed by comparing Eqs. (27) and (28). The reason for this can be explained as follows. In both cases, ambiguities at epoch k are estimated based on the time-averaged phase observables, corrected for the ionospheric spatial gradient estimator at epoch k. Looking at Table 4, one can see that the variance matrices associated with epoch k of the time-invariant ionospheric spatial gradient and the time-variant one are approximately the same. as long as the ambiguities are float, time-variant ionospheric spatial gradient is estimated using code observables (uncorrelated with the phase measurements), and time-invariant ionospheric spatial gradient is estimated using code and time-differenced phase observables (uncorrelated with the time-averaged phase measurements). Therefore, the precisions of the ambiguities are almost the same for both cases.

4 Summary and conclusions

The detectability of the ionospheric spatial gradient using the test in Eq. (10) depends on various factors summarized below in bullets.

- Increasing the number of receivers and the length of the array would lead to detecting smaller ionospheric spatial gradients with the test in Eq. (10). Regarding the array geometry, we showed that configurations fulfilling $e_n^T B = 0$ will decrease the size of the UMPI MDB. However, if one aims at fixing the DD ambiguities with a high success rate at only one epoch, this array geometry would not be of much help. High ILS success rates will be obtained if the array geometry satisfies $D_n^T B \to 0$, which is not desirable for the MDB size. At the same time, one should keep in mind that if the DD ambiguities are successfully fixed, then the highly precise phase observables will contribute to the precision of the ionospheric spatial gradient, making the MDB size very small.

- Both the variance matrix and the MDB region of the ionospheric spatial gradient are independent of our choice of the reference receiver and reference satellite.

- Increasing the number of satellites will give rise to enhancing the ability to detect smaller ionospheric spatial gradients. The higher the elevation of the satellites in view, the better the detectability of the ionospheric spatial gradient will be. Given a satellite configuration, the best ionospheric spatial gradient detectability will be obtained when the ionospheric front affects satellite c of which the elevation-dependent weight w^c is the closest to $\sum_{s=1,s\neq c}^{m} w^s$. The behavior of the precision of the DD ambiguities with respect to the number of satellites and the satellites elevation can be explained the same way.

- Having GNSS observables on more than one frequency available would be of much help in terms of reducing the minimal detectable ionospheric spatial gradient.

- Involving the observables of more than one epoch, say k epochs, has different effects for different scenarios. When the ionospheric spatial gradient is considered to be time-invariant, as long as the ambiguities are float, only the code observable of k epochs contribute to the estimation of the ionospheric spatial gradient, improving its precision by almost k factor and reducing the corresponding MDB size by $\sqrt{k}$. Once the DD ambiguities are successfully fixed, phase observables also play role in the precision of the ionospheric spatial gradient, and enhance it by $\varepsilon = 10^{-4}$ and the associated MDB by $\sqrt{\varepsilon}$ compared with the ambiguity-float scenario.

- When the ionospheric spatial gradient is assumed to change over time, its precision at each epoch will not benefit from observables of other epochs, if only the code observables are included. As the phase measurements are taken into account, and ambiguities are float, the precision and the MDB improve by k and $\sqrt{k}$, respectively. Once the ambiguities are fixed, the precision and the MDB region enhance by, respectively, ε and $\sqrt{\varepsilon}$ with respect to multi-epoch code-only scenario.

Based on the numerical results obtained, when the ambiguities are still float, even if there are 8 symmetrically-distributed receivers with the length of 500 meter, and GNSS observables are available on 2 ($L1$ and $L2$) frequencies, the ionospheric spatial gradient smaller than 6000 mm/km and 1260 mm/km can not be detected with $P_{fa} = 10^{-4}$ and $P_{md} = 10^{-4}$ at single epoch when, respectively, $\sigma_p = 1$ meter and $\sigma_p = 0.2$ meter. The MDB region can become desirable by making the array larger. For example, if the length of the array (the radius of the array circle) reaches 2000 meter, then the previous numbers would reduce to 1500 mm/km and 315 mm/km.

Our outcomes showed that for an array configuration with 4 antennas satisfying $D_n^T B \to 0$, the DD ambiguities could be fixed during a few number of epochs for dual-frequency scenario and $\sigma_p = 0.2$ meter. When $\sigma_p = 1$ meter, however, a large number of epochs are needed for the ILS success rate to reach a desirable value. For example, for a satellite geometry with highly-elevated satellites, when the data sampling-rate is 30 seconds, it would be 25 epochs, and for a satellite geometry with low-elevated satellites, it would be 37 epochs, to get ILS success rate more than 99.9999% when the ionospheric spatial gradient is assumed to change over time. If the ambiguities, by choosing an appropriate array configuration, could be fixed during a few number of epochs, the MDB size would reach values at the level of a few hundred mm/km.

Acknowledgements

This work has been done in the context of the Positioning Program Project 1.19 "Multi-GNSS PPP-RTK Network" of the Cooperative Research Centre for Spatial Information (CRC-SI).

References

[1] G. Seeber, "Satellite geodesy: foundations, methods, and applications," *Berlin; New York: W. de Gruyter, 1993.*, vol. 1, 1993.

[2] B. Hofmann-Wellenhof, H. Lichtenegger, and E. Wasle, *GNSS–global navigation satellite systems: GPS, GLONASS, Galileo, and more*. Springer Science & Business Media, 2007.

[3] H. Bourne and Y. Morton, "GPS receiver ionosphere error correction based on spatial gradients and IGS satellite DCBs," in *Proceedings of the ION 2013 Pacific PNT Meeting, Honolulu, Hawaii, April 2013*, pages 685–693, 2013.

[4] C. Wang and Y. Morton, "Ionosphere TEC and TEC gradients estimation using a regional GNSS network," in *Proceedings of the 26th International Technical Meeting of The Satellite Division of the Institute of Navigation (ION GNSS+ 2013), Nashville, TN, September 2013*, pages 1875–1880, 2013.

[5] C. Wang, J. Wang, and Y. Morton, "Regional ionospheric TEC gradients estimation using a single GNSS receiver," in *China Satellite Navigation Conference (CSNC) 2014 Proceedings: Volume II*, pages 363–373, Springer, 2014.

[6] N. Blaunstein and E. Plohotniuc, *Ionosphere and applied aspects of radio communication and radar*. CRC Press, 2008.

[7] L. Gratton and B. Pervan, "Airborne and ground monitors for ionospheric front detection for the local area augmentation system using carrier phase measurements," in *Proceedings of the 18th International Technical Meeting of the Satellite Division of The Institute of Navigation (ION GNSS 2005), Long Beach, CA, September 2005*, pages 748–757, 2005.

[8] M. Luo, S. Pullen, J. Dennis, H. Konno, G. Xie, T. Walter, P. Enge, S. Datta-Barua, and T. Dehel, "LAAS ionosphere spatial gradient threat model and impact of LGF and airborne monitoring," *Proceedings of ION GPS 2003*, pages 9–12, 2003.

[9] S. Pullen, Y. S. Park, and P. Enge, "Impact and mitigation of ionospheric anomalies on ground-based augmentation of GNSS," *Radio Science*, vol. 44, no. 1, 2009.

[10] D. Simili and B. Pervan, "Code-carrier divergence monitoring for the GPS local area augmentation system," in *Position, Location, And Navigation Symposium, 2006 IEEE/ION*, pages 483–493, 2006.

[11] B. Belabbas, P. Remi, M. Meurer, and S. Pullen, "Absolute slant ionosphere gradient monitor for GAST-D: Issues and opportunities," in *Proceedings of the 24th International Technical Meeting of The Satellite Division of the Institute of Navigation (ION GNSS 2011), Portland, OR, September 2011*, pages 2993–3002, 2011.

[12] G. Giorgi, P. Henkel, and C. Gunther, "Testing of a statistical approach for local ionospheric disturbances detection," in *Proceedings of the IEEE-ION PLANS, Myrtle Beach, SC, USA*, pages 167–173, 2012.

[13] J. Jing, S. Khanafseh, F.-C. Chan, S. Langel, and B. Pervan, "Detecting ionospheric gradients for

GBAS using a null space monitor," in *Proceedings of the IEEE-ION PLANS, Myrtle Beach, SC, USA,*, pages 1125–1133, 2012.

[14] S. Khanafseh, S. Pullen, and J. Warburton, "Carrier phase ionospheric gradient ground monitor for GBAS with experimental validation," *Journal of The Institute of Navigation*, vol. 59, no. 1, pages 51–60, 2012.

[15] M.-S. Circiu, M. Felux, P. Remi, L. Yi, B. Belabbas, and S. Pullen, "Evaluation of dual frequency GBAS performance using flight data," in *Proceedings of the 2014 International Technical Meeting of The Institute of Navigation, San Diego, California*, pages 645–656, 2014.

[16] W. T., "The future of satellite navigation for aviation," *Stanford's 2011 PNT Challenges and Opportunities Symposium*, 2011.

[17] P. J. G. Teunissen and P. F. De Bakker, "Single-receiver single-channel multi-frequency GNSS integrity: outliers, slips, and ionospheric disturbances," *Journal of Geodesy*, vol. 87, no. 2, pages 161–177, 2013.

[18] A. Khodabandeh and P. J. G. Teunissen, "Single-Epoch GNSS Array Integrity: an Analytical Study," *IAG Symp*, vol. 142, 2015. Accepted for publication.

[19] W. Baarda, "A testing procedure for use in geodetic networks," *Publications on geodesy (ISSN 0165-1706*, vol. 2, no. 5, 1968.

[20] P. J. G. Teunissen, *Testing theory, an introduction*. Delft University Press, Delft, The Netherlands, 2001.

[21] J. Magnus, "Linear structures. London School of Economics and Political Science, Charles Griffin & Company LTD," 1988.

[22] H. J. Euler and C. C. Goad, "On optimal filtering of GPS dual frequency observations without using orbit information," *J. Geod.*, vol. 65, no. 2, pages 130–143, 1991.

[23] M. Felux, J. Lee, and F. Holzapfel, "GBAS ground monitoring requirements from an airworthiness perspective," *GPS Solutions*, pages 1–9, 2014.

[24] J. R. Christie, P.-Y. Ko, A. Hansen, D. Dai, S. Pullen, B. S. Pervan, and B. W. Parkinson, "The effects of local ionospheric decorrelation on LAAS: theory and experimental results," pages 769–777, 1999.

[25] P. J. G. Teunissen and A. Kleusberg, *GPS for Geodesy*. Berlin; New York: Springer, second ed., 1998.

[26] T. Murphy, M. Harris, S. Pullen, B. Pervan, S. Saito, and M. Brenner, "Validation of ionospheric anomaly mitigation for GAST-D," *ICAO NSP Working Group of the Whole (WGW) Meeting, Montreal, Canada, WGW/WP 14*, 2010.

[27] B. Belabbas and M. Meurer, "Carrier phase and code based absolute slant ionosphere gradient monitor for GBAS," in *Proceedings of the Institute of Navigation, Nashville, TN, USA*, pages 2201–2208, 2012.

[28] P. J. G. Teunissen, "The least-squares ambiguity decorrelation adjustment: a method for fast GPS integer ambiguity estimation," *Journal of Geodesy*, vol. 70, no. 1-2, pages 65–82, 1995.

[29] P. J. G. Teunissen, "An optimality property of the integer least-squares estimator," *Journal of Geodesy*, vol. 73, pages 587–593, 1999.